View metadata, citation and similar papers at core.ac.uk

brought to you by CORE

provided by Carolina Digital Repository

HHS Public Access

Author manuscript

IEEE Trans Ultrason Ferroelectr Freq Control. Author manuscript; available in PMC 2017 July 12.

Published in final edited form as:

IEEE Trans Ultrason Ferroelectr Freq Control. 2015 September ; 62(9): 1623–1633. doi:10.1109/TUFFC.2014.006883.

Dual Frequency Acoustic Droplet Vaporization Detection for Medical Imaging

Christopher B. Arena[*] **[Member, IEEE]**, **Anthony Novell**[*], **Paul S. Sheeran [Member, IEEE]**, **Connor Puett**, **Linsey C. Moyer**, and **Paul A. Dayton [Member, IEEE]**

University of North Carolina/North Carolina State University Joint Department of Biomedical Engineering, Chapel Hill, NC, 27599 USA

Abstract

Liquid-filled perfluorocarbon droplets emit a unique acoustic signature when vaporized into to gas-filled microbubbles using ultrasound. Here, we conducted a pilot study in a tissue-mimicking flow phantom to explore the spatial aspects of droplet vaporization and investigate the effects of applied pressure and droplet concentration on image contrast and axial and lateral resolution. Control microbubble contrast agents were used for comparison. A confocal dual-frequency transducer was used to transmit at 8 MHz and passively receive at 1 MHz. Droplet signals were of significantly higher energy than microbubble signals. This resulted in improved signal separation and high contrast-to-tissue ratios (CTR). Specifically, with a peak negative pressure (PNP) of 450 kPa applied at the focus, the CTR of B-mode images was 18.3 dB for droplets and −0.4 for microbubbles. The lateral resolution was dictated by the size of the droplet activation area, with lower pressures resulting in smaller activation areas and improved lateral resolution (0.67 mm at 450 kPa). The axial resolution in droplet images was dictated by the size of the initial droplet and independent of the properties of the transmit pulse (3.86 mm at 450 kPa). In post-processing, time-domain averaging (TDA) improved droplet and microbubble signal separation at high pressures (640 kPa and 700 kPa). Taken together, these results indicate that it is possible to generate high-sensitivity, high-contrast images of vaporization events. In the future, this has the potential to be applied in combination with droplet-mediated therapy to track treatment outcomes or as a stand-alone diagnostic system to monitor the physical properties of the surrounding environment.

Index Terms

acoustic droplet vaporization; phase change contrast agent; contrast enhanced ultrasound; tissue characterization; nanodroplet; nanoemulsions; perfluorocarbon

I. Introduction

Ultrasound is a widely used imaging modality primarily due to its ability to capture images in real-time without exposing the interrogated tissue to ionizing radiation. Additionally, ultrasound systems are relatively low cost and portable, making them useful in a variety of clinical settings. In a pulse-echo fashion, images are constructed from backscattered signals

[*]Denotes equal contribution.

Author Manuscript

Author Manuscript

Author Manuscript

Author Manuscript

Author Manuscript Author Manuscript Author Manuscript Author Manuscript

from tissue components. Therefore, anatomical features exhibiting poor scattering cannot readily be detected. For example, perfusion differences that exist between diseased and normal tissues, such as in the case of a highly vascularized tumor, cannot be quantified with standard brightness mode (B-mode) imaging, because blood is a poor scatterer.

To image the vasculature, the acoustic properties of blood can be modified by injecting microbubble contrast agents [1]. These particles typically consist of a gas core encapsulated by an albumin, galactose, polymer, or lipid shell [2]. Introducing a gaseous component into the blood enhances its echogenicity. When insonified, microbubbles oscillate in a non-linear manner and may generate second harmonic [3], super-harmonic [4], and sub-harmonic [5] frequency components. This has given rise to many bubble-specific imaging strategies, including pulse inversion [6], amplitude modulation [7], cadence imaging (combination of pulse inversion and amplitude modulation) [8], chirp reversal [9], and dual-frequency superharmonic imaging [10, 11].

Despite the significant advancements in ultrasonic imaging afforded by the use of microbubbles, size and circulation limitations restrict their application space to short-lived studies within the vascular compartment. Specifically, microbubbles are too large (1–10 μm diameter [12]) for extravasation through cell-to-cell junctions (0.1–0.8 μm spacing in diseased tissue [13]). This prevents the interrogation of extravascular molecular markers or accumulation via the enhanced permeability and retention effect in tumors. A short circulation half-life (1–10 min [12]) precludes the application of microbubbles in long-duration studies, where it is desirable to perform contrast enhanced imaging or therapy mediated by the contrast agent for up to 1 hr without re-dosing. Examples may include using microbubbles to monitor coagulation necrosis during radiofrequency ablation [14] or microbubble-mediated blood-brain-barrier barrier disruption of large volumes greater than $1cm^3$ [15].

To permeate tumor tissue and/or improve circulation time, researchers have been exploring the use of liquid-filled droplets that undergo a phase change to gas-filled microbubbles when subject to a sufficient negative pressure, a process referred to as acoustic droplet vaporization. These phase change contrast agents can be produced with microscale diameters (3–6 μm [16]) for intravascular applications or nanoscale diameters (200–600 nm [17]) for extravascular applications. While in the liquid state, certain droplet formulations have been shown to remain stable *in vivo* for at least 96 min [18]. Once insonified and transitioned into microbubbles, they exhibit sufficient scattering cross-section to yield measureable levels of contrast [19, 20]. The recent development of a new method for condensing microbubbles into droplets has simplified the fabrication process [21, 22]. Additionally, it permits the use of volatile, low-boiling point perfluorocarbons as the core material, which allows for vaporization of sub-micron agents with pressures that are safe for diagnostic imaging [23].

The majority of studies on droplets have focused on therapeutic applications, such as vessel occlusion [16, 24, 25], drug delivery [26–28], and enhancement of thermal [29–31] and non-thermal [32] ablation. The rapid expansion in volume during the vaporization process (5–10 times the original diameter in an un-degassed environment [17]) along with the

Author Manuscript Author Manuscript Author Manuscript Author Manuscript

spatiotemporal control of vaporization using focused pulses can be tuned to produce the desired bioeffect. There is also a growing level of interest in using droplets for diagnostic applications. To date, studies have been conducted on phase aberration correction [25], wash-out characterization of kidney imaging [33], intravascular molecular imaging by targeting alpha(v)-integrins [34], and extravascular imaging through passive accumulation in tumors [20]. All of these techniques are designed to image the microbubbles generated from activated droplets using conventional B-mode or microbubble specific imaging techniques. However, there may be information contained within the vaporization event itself that, if captured, could enable new diagnostic applications or methods of monitoring therapeutic outcomes.

Using high-speed video microscopy, Sheeran *et al.* found that activated droplets initially over-expand and then settle to a final microbubble resting diameter in a oscillatory manner [35]. Additionally, by using a ‘pulse-high’ (8 MHz) ‘listen-low’ (1 MHz) methodology to isolate vaporization signals, it was determined that this process produces a unique acoustic signature resembling an exponentially decaying sinusoidal signal. The amplitude of the sinusoidal signal is greater for larger droplets, as they displace more fluid upon activation. Further, the frequency of the signal is dictated by the final microbubble diameter, with smaller bubbles oscillating at higher frequencies according to equations for a damped harmonic oscillator undergoing un-forced oscillation [36]. Therefore, it may be possible to detect physical properties of both the encapsulating shell and the surrounding environment (such as ambient pressure, temperature, and viscosity), that manifest as alterations in bubble oscillation.

Here, we utilize the ‘pulse-high, listen-low’ strategy employed by Sheeran *et al.* [35] to develop an imaging system for capturing droplet vaporization events and generating ultrasound images. We explore the spatial aspects of vaporization and determine the inherent trade-offs between the applied pressure and image resolution. Droplets and microbubbles are imaged inside a microcellulose tube embedded within a tissue-mimicking phantom to study the effects of attenuation. This represents an extension of our previous feasibility study, which constructed images of a tube in a water bath [37].

The results presented herein indicate that high-contrast images can be created from vaporization signals inside a tissue phantom. The lateral resolution decreases with increasing applied pressure. This is due to the fact that the droplet activation area limits the lateral resolution, and the activation area increases with increasing pressure. The axial resolution is dictated by the exponential decay rate in the vaporization signal. Additionally, post-processing techniques such as time-domain averaging (TDA) and energy detection were able to improve the separation of vaporization signals from signals corresponding to control microbubbles oscillation.

II. Methods

A. Microbubble and Droplet Fabrication

Microbubbles were generated with a lipid shell encapsulating an octafluoropropane (OFP; boiling point −36.7 °C) gas core, as previously described [38]. This formulation is similar to

Author Manuscript Author Manuscript Author Manuscript Author Manuscript

that of DEFINITY®, which has been FDA approved for echocardiography in that it involves a high molecular weight perfluorocarbon and lipid shell. Briefly, a 9:1 M dissolution of 1,2-distearoyl-sn-glycero-3-phosphocholine (DSPC) and 1,2-distearoyl-sn-glycero-3-phosphoethanolamine-N-methoxy (polyethylene-glycol)-2000 (DSPE-PEG2000) was formed in a 16:3:1 excipient solution of phosphate-buffered saline (PBS), propylene glycol, and glycerol for a total lipid concentration of 1 mg/ml. Lipids were purchased from Avanti Polar Lipids (Alabaster, AL, USA). 1.5 ml of the lipid solution was aliquoted into 3 ml glass vials and gas exchanged with OFP (FluoroMed, Round Rock, TX, USA) to replace the free and dissolved air. To generate microbubbles, vials were mechanically agitated (Vialmix, Bristol-Myers Squibb, New York, NY, USA) for 45 s, which resulted in a polydisperse distribution. These microbubbles were used in control experiments.

To form droplets, microbubbles were condensed into droplets according to established techniques [38]. Following mechanical agitation, the vials were submerged in an isopropanol bath maintained at approximately −10 °C and swirled gently for 2 min. While remaining in the bath, the vials were connected to an adjustable air-pressure source, and the headspace pressure was increased to ensure that the majority of the microbubbles visibly converted to droplets. This required pressures on the order of 50 psi. Vials were then stored for no more than 30 min at 4 °C prior to use.

B. Microbubble and Droplet Characterization

Droplets were characterized using a NanoSight NS500 (Malvern Instruments Inc., Westborough, MA, USA). Samples were diluted 1:200 in PBS. Six, 30 s recordings were captured from each vial at 23.3°C with a viscosity of 0.924 cP and detection threshold of 9. The six concentration and size measurements from each vial were averaged to form one representative sample, and the entire process was repeated for a total of 3 vials. Then, the measurements from each vial were averaged together. The averaged distribution of droplets had a mean diameter of 157 ± 9 nm, mode size of 111 ± 10 nm, and total concentration of $2.38\times10^{11} \pm 1.07\times10^{11}$ particles/ml. Reproducibility between vials was high for the mean and modal diameter. The NanoSight was unable to detect content larger than ~500 nm, because the measurements were dominated by the peak at 111 nm.

An AccuSizer 780A (Particle Sizing Systems, Port Richey, FL, USA) capable of measuring particles ranging in size from 0.5 to 500 μm, was used to observe larger droplet content, and to characterize microbubbles. For microbubbles, 2 μl of the sample was injected into 50 ml of deionized water in the dilution flask. For droplets, a larger volume of 50 μl was required to compensate for the fact that most of the particles were submicron in size. Three trials were performed per vial, and the statistics were averaged to form one representative sample. Then, the measurements from three separate vials were averaged together. The averaged distribution of droplets had a mean diameter of 0.98 ± 0.10 μm, mode size of 0.58 ± 0.01 μm, and total concentration of $2.77\times10^{8} \pm 3.04\times10^{6}$ particles/ml. The concentration of larger droplet content observed by the AccuSizer was approximately three orders of magnitude smaller than that of content less than 0.5 μm observed by the NanoSight. The averaged distribution of control microbubbles had a mean diameter of 1.02 ± 0.03 μm, mode size of 0.59 ± 0.01 μm, and total concentration of $1.11\times10^{10} \pm 3.32\times10^{9}$ particles/ml.

Author Manuscript Author Manuscript Author Manuscript Author Manuscript

C. Experimental Setup and Phantom Creation

A dual-frequency transducer design was utilized that consisted of two confocal piston transducers (Fig. 1). The inner element was used to transmit a 2 cycle, high-frequency (8 MHz) Gaussian enveloped sinusoid (7.5 MHz center frequency, 1.27 cm diameter, 5.08 cm focus; V320, Panametrics Inc., Waltham, MA, USA). The outer element was used to passively receive at low-frequency (1 MHz center frequency, 3.81 cm diameter, 5.08 cm focus; V30047, Panametrics Inc., Waltham, MA, USA). Transmit pulses were applied at a repetition rate of 10 Hz with excitation signals from an arbitrary function generator (AFG 3101, Tektronix, Beaverton, OR, USA) that were amplified with a 60 dB power amplifier (A-500, ENI, Rochester, NY, USA). Transducer calibration was performed in the free-field at the focus using a needle hydrophone (HNA-0400, Onda Corp., Sunnyvale, CA, USA) to obtain pressure output information. Received signals were filtered (0.1 MHz to 3 MHz band-pass) and amplified (32 dB) using a broadband receiver (BR-640A, RITEC Inc., Warwick, RI, USA). Then, A/D conversion was performed at a 100 MHz sampling rate using a 14-Bit waveform digitizer (PDA14, Signatec, Lockport, IL, USA) controlled by LabVIEW (National Instruments, Austin, TX, USA).

The tissue-mimicking phantom tested in this study was constructed by embedding a microcellulose tube (~220 μm inner diameter) inside a gellan gum base material. The tube was included to simulate a micro blood vessel, through which contrast agent could be infused. The base material was similar to that described in [39], which was originally developed for high-intensity focused ultrasound, except that graphite powder (13.5 g) was used as the scattering medium in lieu of aluminum oxide particles (6.75 g in the original recipe). The other components of the recipe (gellan gum, calcium chloride, potassium sorbate, and propanol) remained the same. Following mixing of the components and while in the liquid state (70°C), the phantom was poured into a mold containing the microcellulose tube and allowed to solidify during the cooling process.

Attenuation coefficients of the phantom were measured by the through-transmission substitution technique [40] for eight discrete frequencies (from 1 to 8 MHz). Acoustical measurements were performed before and after insertion of the phantom in a degassed-water tank maintained at 37°C. Ultrasound waves were generated from three different focused single-element transducers (V30047, V382, V320, Panametrics Inc., Waltham, MA) focused at 50 mm and centered at 1 MHz, 3.5 MHz and 7.5 MHz to cover the full range of frequencies. Transducers were driven with the same arbitrary function generator and amplifier arrangement as previously described. For each frequency, a 10-cycle excitation tone burst was transmitted at a peak negative pressure (PNP) less than 160 kPa at the focus to avoid undesirable nonlinear propagation. The delivered excitation pulses were measured using the needle hydrophone placed at the focal distance of the transducers. The pulses received by the hydrophone were captured with the A/D converter, and data was transferred to MATLAB (R2013b, The Mathworks, Natick, MA, USA) for offline analysis. Both the hydrophone and transducers were mounted on a holder to be static during the experiment. For attenuation measurements (Table I), the phantom was positioned in front of the transducer as closely as possible to the hydrophone. The attenuation coefficient (dB per unit length) at frequency, f was given by the equation:

Author Manuscript Author Manuscript Author Manuscript Author Manuscript

$$\alpha(f)=(10/d)\log 10[E_0/(E)] \quad (1)$$

where d is the phantom thickness, and E_0 and E are the energy of the signal propagated in water and through the phantom, respectively. The ultrasound attenuation exhibits a frequency dependent relationship as:

$$\alpha(f)=Af^n \quad (2)$$

where A = 0.24 ± 0.02 dB.cm^{-1}.MHz^{-1} and n = 1.46. The attenuation coefficient of the phantom was on the same order of magnitude as typical attenuation values measured for blood (0.09–0.17 dB.cm^{-1}.MHz^{-1}) and fatty tissue (0.38–0.78 dB.cm^{-1}.MHz^{-1}) [41].

D. Data Acquisition and Image Processing

The stand-alone microcellulose tube and tissue phantom were placed in heated (37°C) degassed water at the transducer focus. The stock solutions of microbubbles and droplets were diluted in PBS (0.03% and 0.3% v/v) and continuously infused through the tube at 50 μl/min using a syringe pump (PHD2000, Harvard Apparatus, Holliston, MA, USA) to ensure that the activated volume did not interfere with subsequent pulses. LabVIEW was used to raster the transducer in the elevational (4 mm, 121 μm step size) and lateral (3 mm, 125 μm step size) dimensions. At each location, five radiofrequency (RF) lines were acquired and stored for offline analysis. In the tissue phantom, the PNPs at the focus were 160, 450, 640, 700, and 770 kPa (after accounting for attenuation).

Images were created from the stored RF data using a custom MATLAB script. A 3rd order Butterworth filter was applied to isolate vaporization signals (400 kHz to 1.6 MHz band-pass). After filtering, two types of images were generated, including conventional B-mode images in the axial-lateral plane and energy projections (EPs) in the lateral-elevational plane. In the case of the B-mode images, the center slice through the tube was selected, and the highest intensity signal was selected out of the five received at each lateral position. Then, the envelope of the signal was taken (absolute value of the Hilbert transform), converted to a decibel scale, and plotted. In the case of the EPs, the energy was calculated as the summation of squared signals within a 12 μs window surrounding the five signals received at each lateral-elevational position. Then, the highest energy signal was selected as the representative pixel value at that position and projected onto the lateral-elevational plane. Energy was chosen as an initial method to separate vaporization events from control microbubble signals, because vaporization signals possess significantly higher energy at low mechanical index, as noted by their long tails (see Fig. 2a). In all images, pixel values were linearly interpolated on a refined grid formed by dividing the interval between pixels three times in each dimension.

The contrast-to-tissue ratio (CTR) was calculated in the B-mode and EP images. In the B-mode images, the energy outside the tube was subtracted from the energy inside the tube, for each pixel row, and the results were averaged to obtain a single value. The energy was

Author Manuscript Author Manuscript Author Manuscript Author Manuscript

calculated as the summation of squared signals within a 12 μs window at each lateral position. The window was centered around the tube to measure the signal from contrast agents, or located directly in front of the tube to measure tissue signals. In the EP images, the average pixel value outside the tube was subtracted from the average pixel value inside the tube, for each pixel column, as pixel values were already in units of energy. These results were then averaged to obtain a single value. The region outside the tube was located at the maximum elevational distance above the tube, and the region inside the tube was located around the central elevational slice. The specified regions of interest in B-mode and EP images are shown as red dotted lines in Figs. 3 and 4, respectively.

The axial resolution was calculated based on the enveloped and log compressed signals acquired during each trial. The signals were normalized to their maximum value, and the −6 dB point from the peak was selected as the threshold pixel value for defining the distance associated with the axial resolution. Data exhibiting a poor signal-to-noise ratio (*i.e.*, < 6dB) were not included in axial resolution calculations.

The tube width at −10 dB was calculated for each pixel column within an EP image, and the results were averaged to obtain a single value. Pixel values were interpolated with splines using ten query points per pixel. Additionally, RF lines that contained noisy signals or a −10 dB point that fell within the baseline noise were excluded from calculations.

Time domain averaging (TDA) was investigated as a secondary method for improving the separation of droplet and microbubble signals in B-mode and EP images. The five RF lines received at each location were averaged, and then the average RF line was subtracted from each individual receive line prior to envelope detection and energy calculations. This technique has been studied as a way to reject clutter during color Doppler imaging [42], as signals that are relatively constant and appear in each receive line are removed. In the case of droplet activation, vaporization signals vary in amplitude, frequency, and phase to a greater extent than microbubble and tissue signals received at 1/8 the insonification frequency. This is due to the stochastic nature of droplet activation (i.e., not all transmit events induce vaporization, even when the PNP is above the threshold for activation) as well as the dependence of the vaporization signal on droplet size.

One-way ANOVA was used to investigate the effects of contrast agent formulation, concentration, and applied pressure on the axial resolution and apparent tube width. The analysis was performed on non-TDA datasets. In the event of a significant main effect, pairwise comparisons were completed using Tukey’s Honestly Significant Difference (HSD). A similar analysis was conducted for CTR calculations in B-mode and EP images, with and without TDA. All statistical analyses were conducted using Minitab Express (Minitab, State College, PA, USA) with a significance level of $p < 0.05$.

III. Results

Droplet activation resulted in exponentially decaying sinusoidal signals in the time-domain (Fig. 2a). The initial peak is caused by the rapid expansion in droplet diameter during vaporization, and the decaying oscillatory tail is caused by the oscillation of the generated

Author Manuscript Author Manuscript Author Manuscript Author Manuscript

microbubbles around their final resting diameter [35]. The amplitude and length of the signals varied between events, even at constant pressure. Signals from control microbubbles were more consistent in amplitude within a given pressure group, and lacked the oscillatory tail feature. The frequency of the droplet signals also varied between events, and the spectrum was distinctly more narrowband compared to microbubble trials (Fig. 2b). Microbubbles excited by the 8 MHz transmit pulse return a wideband echo to the 1 MHz receive transducer that caused it to ring at its center frequency. Alternatively, peaks in droplet frequency correspond to the rate at which newly generated microbubbles oscillate around their final diameter. Over the course of the experiments, peaks in the droplet spectrum were observed primarily in the range of frequencies corresponding to the receiving transducer bandwidth, between 400 kHz and 1.6 MHz. The band-pass filter was used to isolate this frequency content.

B-mode images at 700 kPa are shown in Fig. 3. The oscillatory behavior of activated droplets resulted in hyperechoic streaks extending away from the tube in the direction of the transmit pulse propagation. The high droplet concentration (0.3%) increased the number of vaporization events, and prevented the presence of gaps in the tube image that were seen at the low concentration (0.03%). Gaps result from locations where no droplet vaporization was produced, due to the stochastic nature of droplet activation. B-mode images from control microbubbles resulted in a sharply defined, hyperechoic tube at 0.3% concentration. The TDA technique effectively reduced the signals from microbubbles and the water-phantom boundary while maintaining the signals from droplets. For 0.03% concentration post-TDA, it was possible to obtain a clear image from droplet activation (CTR = 18.1 dB) while completely removing the microbubble signals (CTR = 0.4 dB). CTR calculations for 0.3% concentration at all pressures tested are presented in the last paragraph of the results section (see Fig. 6).

The axial resolution in the case of microbubbles was approximately 2 mm, and there was no significant effect of the applied pressure (Table II). This value is partially dictated by the impulse response of the receive transducer. As the microbubble concentration was reduced, the axial resolution deteriorated, but not significantly so (higher values correlate to poorer resolution, and vice versa). This result is attributed to a reduction of the signal-to-noise ratio degrading the axial resolution measurement at −6 dB. At 700 kPa, the axial resolution in the case of droplets at 0.3% and 0.03% concentrations were significantly worse than microbubbles at 0.3% concentration. However, the 0.3% concentration of droplets had significantly better resolution than the 0.03% concentration of droplets. For the case of droplets, the axial resolution is directly linked to the decay rate of the vaporization signal. Higher frequency signals (*i.e.*, those produced from smaller droplets/bubbles) decay faster and correlate to improved axial resolution.

EP images are shown in Fig. 4. Here, the oscillatory behavior of droplets was integrated and projected onto the lateral-elevational plane. This resulted in well-defined boundaries between the tube and surrounding tissue phantom. As in the case of B-mode images, the high droplet concentration (0.3%) increased the number of vaporization events, and prevented the presence of gaps in the tube image that were seen at the low concentration (0.03%). Increasing the pressure caused the tube to appear wider (Fig. 5). This can be

Author Manuscript Author Manuscript Author Manuscript Author Manuscript

explained by the fact that at higher applied pressures, activation could be achieved further from the tube (see Fig. 7 in section IV). At 450 kPa, the apparent tube width in the case of 0.3% droplet concentration was 0.67 mm. When taken as a measure of the lateral resolution, this was significantly better than when higher pressures were applied to droplets or microbubbles at the same concentration (~1.5 mm). There was no significant difference in the apparent tube width between droplets at 0.3% and 450 kPa, and droplets at 0.03% and 640 kPa. This suggests that lowering the concentration raises the threshold for activation [43]. It was not possible to generate reliable measures of tube width from microbubbles at concentrations of 0.03%, even at the highest pressures tested, as the backscattered signal was too weak relative to the tissue signal. Microbubbles at 0.3% and 700 kPa resulted in wider tube calculations than noted visually, due to reduced CTR and spreading of the −10 dB point.

CTR calculations for B-mode and EP images at 0.3% concentration are shown in Fig. 6. A steep increase in CTR occurs when the PNP rises above the threshold pressure for droplet activation (between 160 and 450 kPa). Droplet activation is an all-or-nothing phenomenon, and increases in pressure well above the threshold result in only slight gains in CTR at the expense of reduced lateral resolution. Microbubbles exhibit a more gradual rise in CTR with pressure. However, even at the highest achievable acoustic pressure amplitude (700 kPa), the CTR from microbubbles was significantly lower than the CTR from droplets. Additionally, at 700 kPa, the TDA technique was able to significantly reduce the CTR from microbubbles, while having no significant impact on the CTR from droplets. In the B-mode images, the variability (error bars) of the CTR from droplets increased at 450 kPa due to the presence of signal gaps. When TDA was combined with the EP technique, it was possible to completely separate droplet signals from microbubble signals at 0.3% concentration and 640 kPa (CTR = 22.68 for droplets and CTR = 0.50 for microbubbles). At lower pressures, no TDA or EP was required to separate these signals in the phantom.

IV. Discussion

Here, we demonstrate that droplet activation signals can be detected and extracted from microbubble and tissue signals to produce high contrast images. The specificity of the approach is based on the detection of the low frequency echo that occurs during droplet vaporization (see Fig. 2), which results from the oscillation of generated microbubbles around their final resting diameter. The large difference between the activation pulse frequency (*i.e.*, 8 MHz) and the listening frequency (*i.e.*, 1 MHz) results in a weak response from microbubbles and tissue. Additionally, the receive transducer's bandwidth (88% at −6 dB) contributes to signal separation. The microbubble response occurs primarily around the excitation frequency and is reduced at 1 MHz, whereas a portion of the droplet vaporization signals are emitted directly within the bandwidth of the receive transducer. An advantage of imaging droplet vaporization is increased penetration depth, because of the weak attenuation of low frequency droplet content in tissue. Additionally, the contrast enhancement of the technique is also improved by the absence of non-linear propagation in tissue at the listening frequency.

Author Manuscript Author Manuscript Author Manuscript Author Manuscript

Peaks in the droplet spectrum were observed primarily between 400 kHz and 1.6 MHz. According to Sheeran *et al.* [35], this behavior follows the model for a damped harmonic oscillator undergoing un-forced oscillation [36]:

$$f_{\mathrm{damp}}=f_M\sqrt{\frac{1}{1+\left(\frac{\delta}{2}\right)^2}}\ \text{and}\ f_M=\frac{1}{2\pi r}\sqrt{\frac{3\kappa P_l}{\rho_l}} \quad (3, 4)$$

where f_M is the natural resonance frequency, δ is the total damping coefficient (0.76), r is the radius of the generated microbubbles, κ is the polytropic exponent (1.06), P_l is the ambient pressure (101.325 kPa), and ρ_l is the density of the surrounding liquid (994 kg.cm^{-3}). The model predicts that smaller droplets will generate smaller microbubbles that oscillate at higher frequencies when compared to larger droplets. Oscillation frequencies (damped) ranging from 400 kHz to 1.6 MHz correspond to initial droplet diameters ranging from 2.4 μm to 600 nm, respectively. According to the droplet characterization results (see Methods section), this is only a small proportion of the content present in the microcellulose tube. The peak in the droplet distribution occurs at 111 nm, and these droplets would generate microbubbles that oscillate at 8.7 MHz.

Several authors have studied vaporization dynamics using high-speed microscopy [23, 43–45]. Shpak *et al.* describe three distinct regimes, including droplet deformation, rapid growth of vapor bubbles, and slow expansion after ultrasound exposure [45]. When longer pulses (> 5 cycles) were used, forced oscillations of the generated microbubbles during the rapid growth phase were observed, as opposed to the natural response seen here. Doinikov *et al.* has recently developed a comprehensive model to predict the growth of the vapor bubble inside a droplet from the induction stage to the oscillatory stage [46]. This model, which is the result of the underlying fluid dynamics and thermodynamics, explains additional features of droplet activation that were seen experimentally, such as the influence of the perfluorocarbon core material. For example, when using decafluorobutane (DFB), which has a higher boiling point than OFP, the intensity of the impulse wave that occurs at the onset of vaporization is reduced, because the event occurs more slowly. The intensity of the wave front is also reduced for smaller droplets, as they displace less fluid upon activation.

B-mode images (Fig. 3, 40 dB dynamic range) were visibly degraded in the axial dimension compared to the calculated values for axial resolution at −6 dB (Table II). This is due to the greater signal energy present below 6 dB for droplets from generated bubble ringing. Improved axial resolution is possible with the detection of smaller droplets (100–200 nm) that have a higher frequency vaporization signal that decays more rapidly. Additionally, in terms of applications, detection of smaller droplets would improve the systems ability to monitor extravasated nanodroplets. In this study, the oscillation frequency of droplets on the order of 100 nm overlaps with linear reflections from interrogated media (*e.g.*, microbubbles and tissue) and falls far outside the bandwidth of the 1 MHz receive transducer. To view these signals, both the transmit and receive frequency would have to be raised, such that the receive frequency is centered around the droplet oscillation frequency, and the transmit pulse is short enough so as not to influence the oscillation. Nevertheless, a higher transmit

Author Manuscript Author Manuscript Author Manuscript Author Manuscript

frequency (*e.g.*, >20 MHz) may limit the ability to achieve droplet vaporization through a depth of tissue. The TDA approach could represent an alternative option for extracting the signal from smaller droplets. The efficiency of TDA has already been demonstrated to reject clutter during color Doppler imaging [42], and it has been shown here to reduce both the microbubble response at 1 MHz.

Small droplet vaporization signals could be easily detected when activation is induced by pulsed laser irradiation. Recently, Wilson *et al.* have investigated the potential of perfluorocarbon nanodroplets with encapsulated plasmonic nanoparticles for photoacoustic imaging [47]. They reported a substantial increase of the photoacoustic signal during droplet activation. We support that this contrast enhancement corresponds to the detection of the unique acoustic signature from nanodroplet vaporization. Therefore, this photoacoustic signal could be optimized by selecting the listening frequency as close as possible to the resonance frequency of the final microbubbles produced after vaporization [35].

One emerging technique for improving the resolution of ultrasound when operating at low-frequencies relies on the spatial localization of isolated microbubble signals [48–50]. The position of a single microbubble is estimated from time-of-flight or center-of-mass calculations on received signals, and the position density map for multiple microbubble signals can be generated to “paint” out structures wherein the bubbles are confined. This method of super-resolution can overcome the diffraction limit of conventional ultrasound imaging. A similar approach could be applied to droplet imaging in order to improve the axial resolution. The center of mass or peak of the vaporization signal could be used to depict its axial position. Further, the energy of the vaporization signal could be correlated to pixel intensity, as performed here.

The lateral resolution of the droplet imaging system is dictated by the activation area (Fig. 7). At higher applied pressures, the area capable of inducing droplet vaporization increases. As a result, activation can be achieved further from the tube and the apparent tube width increases. To improve the lateral resolution, the activation area should be decreased. This could be accomplished through the use of a linear or phased array transducer with a larger aperture than the piston transducer employed here to better focus the transmit beam. Alternatively, the activation area could be decreased by raising the threshold for droplet activation. Less volatile perfluorocarbon gases could be used for the droplet core, or the concentration of droplets could be reduced. In either of these cases, longer acquisition periods would be required to ensure that a vaporization event was captured at each position to prevent the presence of signal gaps in the reconstructed images.

Droplet activation imaging has the potential to be applied in combination with droplet-mediated therapy or as a stand-alone diagnostic imaging modality. Its utility as a diagnostic will depend largely on the safety of the vaporization event. Microscale droplets have been shown to promote tissue occlusion [16, 24, 25], and nanoscale droplets have been shown to enhance drug delivery [26–28] and tissue ablation [29–32] when long pulses are used to induce cavitation of the generated microbubbles. However, little is known about the bioeffects associated with nanoscale droplets if short pulses are applied for activation without subsequent cavitation. Although maximum expansion of sub-micron droplets is

Author Manuscript Author Manuscript Author Manuscript Author Manuscript

likely less than the diameter of a standard capillary, there remains the possibility of bioeffects due to wall velocity or associated fluid shear. Future studies will be needed to further elucidate the safety of sub-micron droplet activation in-vivo.

When combined with therapy, droplet imaging has the ability to distinguish newly generated microbubbles from microbubbles that were generated from prior activation pulses and remain in circulation. For example, during droplet-mediated high-intensity focused ultrasound, droplet activation is required to enhance thermal energy deposition. Compared to microbubbles, droplets are found to reduce the acoustic energy and time required to cause an ablation [18]. By using ultrasound to monitor the vaporization of fresh droplets in real-time, it would be possible to visualize and control which areas of the tissue are treated versus spared. Furthermore, pressure and temperature play a major role in droplet activation [46]. Detection of the vaporization signal could also be useful in determining whether the PNP and/or the temperature exceed a threshold in a targeted region during treatment [51].

For diagnostic purposes, it may be possible to deduce information about the surrounding environment by examining the droplet vaporization signals. Asami *et al.* have shown that droplet activation behavior is influenced by the viscoelastic properties of a tissue phantom (when the droplets are embedded directly in the phantom) [52]. The peak intensity of the impulse wave was reduced with increasing tissue stiffness. A system designed to monitor this oscillatory behavior could map the tissue stiffness in real-time. In addition to viscoelastic properties, shifts in oscillation frequency may correlate to changes in temperature and pressure. Microbubbles have been shown to exhibit an increased radial excursion at higher temperatures [53] and decreased sub-harmonic response at higher ambient pressures [54]. If possible, correlating these changes with vaporization behavior will likely require a monodisperse population of droplets [55, 56] with a finely tuned oscillation frequency.

The droplet activation detection system was successful at isolating droplet vaporization events from pre-existing, or remnant, microbubbles. This is evident from the higher CTRs seen in both B-mode and EP images of droplet trials compared to microbubble controls (Fig. 6). Further, as the time course of droplet signals varied widely between vaporization events compared to microbubble signals, the TDA approach enhanced signal separation by suppressing microbubble signals while leaving droplet signals largely unchanged. It is important to note that the ‘pulse-high, listen-low’ scheme was designed to exclude microbubble signals. However, many proven microbubble specific imaging techniques for vascular applications, such as pulse inversion [6], amplitude modulation [7], and chirp reversal [9] are capable of generating CTRs in the same range as seen here for droplets [57]. As droplets continue to gain momentum as theranostic agents, the ability to map their conversion to microbubbles in real-time using the dual frequency technique could concurrently become an important tool in clinical practice.

Acknowledgments

The authors thank James K. Tsuruta and Terry O. Matsunaga for insightful discussions and shared expertise on preparing the ultrasound contrast agents. C. B. Arena and L. C. Moyer were supported by a grant from the National Institute of General Medical Sciences, division of Training, Workforce Development, and Diversity under the

Author Manuscript Author Manuscript Author Manuscript Author Manuscript

Institutional Research and Academic Career Development Award, grant #K12-GM000678. A. Novell gratefully acknowledges financial support from Fondation ARC pour la Recherche sur le Cancer (#SAE20130606511). P. S. Sheeran was supported by a graduate research fellowship from the National Science Foundation. Additional research funding was provided by the Focused Ultrasound Foundation and the National Science Foundation through DMR#1122483.

This work was supported in part by the National Science Foundation grant DMR #1122483 through the Materials Interdisciplinary Research Team (MIRT) at the University of North Carolina – Chapel Hill.

References

1. Gramiak R, Shah PM. Echocardiography of the aortic root. Invest Radiol. Sep-Oct;1968 3:356–66. [PubMed: 5688346]
2. Sirsi S, Borden M. Microbubble Compositions, Properties and Biomedical Applications. Bubble Sci Eng Technol. Nov.2009 1:3–17. [PubMed: 20574549]
3. Frinking PJ, Bouakaz A, Kirkhorn J, Ten Cate FJ, de Jong N. Ultrasound contrast imaging: current and new potential methods. Ultrasound Med Biol. Jul.2000 26:965–75. [PubMed: 10996696]
4. Bouakaz A, Krenning BJ, Vletter WB, ten Cate FJ, De Jong N. Contrast superharmonic imaging: A feasibility study. Ultrasound in Medicine and Biology. Apr.2003 29:547–553. [PubMed: 12749924]
5. Shi WT, Forsberg F, Goldberg BB. Subharmonic imaging with gas-filled microbubbles. The Journal of the Acoustical Society of America. 1997; 101:3139–3139.
6. Burns PN, Wilson SR, Simpson DH. Pulse inversion imaging of liver blood flow - Improved method for characterizing focal masses with microbubble contrast. Investigative Radiology. Jan.2000 35:58–71. [PubMed: 10639037]
7. Mor-Avi V, Caiani EG, Collins KA, Korcarz CE, Bednarz JE, Lang RM. Combined assessment of myocardial perfusion and regional left ventricular function by analysis of contrast-enhanced power modulation images. Circulation. Jul 17.2001 104:352–357. [PubMed: 11457757]
8. Bleuzen A, Tranquart F. Incidental liver lesions: diagnostic value of cadence contrast pulse sequencing (CPS) and SonoVue. European Radiology. Oct.2004 14:P53–P62. [PubMed: 15700333]
9. Novell A, van der Meer S, Versluis M, de Jong N, Bouakaz A. Contrast Agent Response to Chirp Reversal: Simulations, Optical Observations, and Acoustical Verification. Ieee Transactions on Ultrasonics Ferroelectrics and Frequency Control. Jun.2009 56:1199–1206.
10. Gessner R, Lukacs M, Lee M, Cherin E, Foster FS, Dayton PA. High-Resolution, High-Contrast Ultrasound Imaging Using a Prototype Dual-Frequency Transducer: In Vitro and In Vivo Studies. Ieee Transactions on Ultrasonics Ferroelectrics and Frequency Control. Aug.2010 57:1772–1781.
11. Gessner RC, Aylward SR, Dayton PA. Mapping microvasculature with acoustic angiography yields quantifiable differences between healthy and tumor-bearing tissue volumes in a rodent model. Radiology. Sep.2012 264:733–40. [PubMed: 22771882]
12. Mullin L, Gessner R, Kwan J, Kaya M, Borden MA, Dayton PA. Effect of anesthesia carrier gas on in vivo circulation times of ultrasound microbubble contrast agents in rats. Contrast Media Mol Imaging. May-Jun;2011 6(3):126–31. [PubMed: 21246710]
13. Prabhakar U, Maeda H, Jain RK, Sevick-Muraca EM, Zamboni W, Farokhzad OC, et al. Challenges and Key Considerations of the Enhanced Permeability and Retention Effect for Nanomedicine Drug Delivery in Oncology. Cancer Research. Apr 15.2013 73:2412–2417. [PubMed: 23423979]
14. Wallace N, Dicker S, Lewin P, Wrenn SP. Influence of nesting shell size on brightness longevity and resistance to ultrasound-induced dissolution during enhanced B-mode contrast imaging. Ultrasonics. Dec.2014 54:2099–108. [PubMed: 25041980]
15. McDannold N, Arvanitis CD, Vykhodtseva N, Livingstone MS. Temporary Disruption of the Blood-Brain Barrier by Use of Ultrasound and Microbubbles: Safety and Efficacy Evaluation in Rhesus Macaques. Cancer Research. Jul 15.2012 72:3652–3663. [PubMed: 22552291]
16. Kripfgans OD, Fowlkes JB, Miller DL, Eldevik OP, Carson PL. Acoustic droplet vaporization for therapeutic and diagnostic applications. Ultrasound in Medicine and Biology. Sep.2000 26:1177–1189. [PubMed: 11053753]

Author Manuscript Author Manuscript Author Manuscript Author Manuscript

17. Sheeran PS, Wong VP, Luois S, McFarland RJ, Ross WD, Feingold S, et al. Decafluorobutane as a Phase-Change Contrast Agent for Low-Energy Extravascular Ultrasonic Imaging. Ultrasound in Medicine and Biology. Sep.2011 37:1518–1530. [PubMed: 21775049]
18. Phillips LC, Sheeran PS, Puett C, Timbie KF, Price RJ, Miller GW, et al. Dual perfluorocarbon nanodroplets enhance high intensity focused ultrasound heating and extend therapeutic window in vivo. The Journal of the Acoustical Society of America. 2013; 134:4049–4049.
19. Forsberg F, Liu JB, Merton DA, Rawool NM, Goldberg BB. Parenchymal Enhancement and Tumor Visualization Using a New Sonographic Contrast Agent. Journal of Ultrasound in Medicine. Dec.1995 14:949–957. [PubMed: 8583531]
20. Williams R, Wright C, Cherin E, Reznik N, Lee M, Gorelikov I, et al. Characterization of Submicron Phase-Change Perfluorocarbon Droplets for Extravascular Ultrasound Imaging of Cancer. Ultrasound in Medicine and Biology. Mar.2013 39:475–489. [PubMed: 23312960]
21. Matsunaga TO, Sheeran PS, Luois S, Streeter JE, Mullin LB, Banerjee B, et al. Phase-Change Nanoparticles Using Highly Volatile Perfluorocarbons: Toward a Platform for Extravascular Ultrasound Imaging. Theranostics. 2012; 2:1185–1198. [PubMed: 23382775]
22. Sheeran PS, Luois S, Dayton PA, Matsunaga TO. Formulation and Acoustic Studies of a New Phase-Shift Agent for Diagnostic and Therapeutic Ultrasound. Langmuir. Sep 6.2011 27:10412–10420. [PubMed: 21744860]
23. Sheeran PS, Matsunaga TO, Dayton PA. Phase-transition thresholds and vaporization phenomena for ultrasound phase-change nanoemulsions assessed via high-speed optical microscopy. Physics in Medicine and Biology. Jul 7.2013 58:4513–4534. [PubMed: 23760161]
24. Kripfgans OD, Orifici CM, Carson PL, Ives KA, Eldevik OP, Fowlkes JB. Acoustic droplet vaporization for temporal and spatial control of tissue occlusion: A kidney study. Ieee Transactions on Ultrasonics Ferroelectrics and Frequency Control. Jul.2005 52:1101–1110.
25. Kripfgans OD, Fowlkes JB, Woydt M, Eldevik OP, Carson PL. In vivo droplet vaporization for occlusion therapy and phase aberration correction. Ieee Transactions on Ultrasonics Ferroelectrics and Frequency Control. Jun.2002 49:726–738.
26. Rapoport N, Nam KH, Gupta R, Gao ZG, Mohan P, Payne A, et al. Ultrasound-mediated tumor imaging and nanotherapy using drug loaded, block copolymer stabilized perfluorocarbon nanoemulsions. Journal of Controlled Release. Jul 15.2011 153:4–15. [PubMed: 21277919]
27. Rapoport N. Phase-shift, stimuli-responsive perfluorocarbon nanodroplets for drug delivery to cancer. Wiley Interdisciplinary Reviews-Nanomedicine and Nanobiotechnology. Sep-Oct;2012 4:492–510. [PubMed: 22730185]
28. Chen CC, Sheeran PS, Wu SY, Olumolade OO, Dayton PA, Konofagou EE. Targeted drug delivery with focused ultrasound-induced blood-brain barrier opening using acoustically-activated nanodroplets. Journal of Controlled Release. Dec 28.2013 172:795–804. [PubMed: 24096019]
29. Puett C, Phillips L, Sheeran P, Dayton P. In vitro parameter optimization for spatial control of focused ultrasound ablation when using low boiling point phase-change nanoemulsions. Journal of Therapeutic Ultrasound. 2013; 1:1–13. 2013/09/13. [PubMed: 24761222]
30. Phillips LC, Puett C, Sheeran PS, Miller GW, Matsunaga TO, Dayton PA. Phase-shift perfluorocarbon agents enhance high intensity focused ultrasound thermal delivery with reduced near-field heating (vol 134, pg 1473, 2013). Journal of the Acoustical Society of America. Dec. 2013 134:4575–4575.
31. Zhang P, Porter T. An in Vitro Study of a Phase-Shift Nanoemulsion: A Potential Nucleation Agent for Bubble-Enhanced Hifu Tumor Ablation. Ultrasound in Medicine and Biology. Nov.2010 36:1856–1866. [PubMed: 20888685]
32. Vlaisavljevich E, Durmaz YY, Maxwell A, ElSayed M, Xu Z. Nanodroplet-Mediated Histotripsy for Image-guided Targeted Ultrasound Cell Ablation. Theranostics. 2013; 3:851–864. [PubMed: 24312155]
33. Sheeran PS, Rojas JD, Puett C, Hjelmquist J, Arena CB, Dayton PA. Contrast-Enhanced Ultrasound Imaging and in Vivo Circulatory Kinetics with Low-Boiling-Point Nanoscale Phase-Change Perfluorocarbon Agents. Ultrasound in Medicine and Biology. 41:814–831.

Author Manuscript Author Manuscript Author Manuscript Author Manuscript

34. Sheeran PS, Streeter JE, Mullin LB, Matsunaga TO, Dayton PA. Toward Ultrasound Molecular Imaging with Phase-Change Contrast Agents: An in Vitro Proof of Principle. Ultrasound in Medicine and Biology. May.2013 39:893–902. [PubMed: 23453380]
35. Sheeran PS, Matsunaga TO, Dayton PA. Phase change events of volatile liquid perfluorocarbon contrast agents produce unique acoustic signatures. Phys Med Biol. Jan 20.2014 59:379–401. [PubMed: 24351961]
36. Minnaert M. XVI. On musical air-bubbles and the sounds of running water. The London, Edinburgh, and Dublin Philosophical Magazine and Journal of Science. 1933; 16:235–248. 1933/08/01.
37. Arena CB, Novell A, Sheeran PS, Puett C, Phillips LC, Dayton PA. Ultrasound Imaging from Vaporization Signals Emitted by Phase Change Contrast Agents. Ultrasonics Symposium (IUS), 2014 IEEE International. 2014
38. Sheeran PS, Luois SH, Mullin LB, Matsunaga TO, Dayton PA. Design of ultrasonically-activatable nanoparticles using low boiling point perfluorocarbons. Biomaterials. Apr.2012 33:3262–3269. [PubMed: 22289265]
39. King RL, Liu YB, Maruvada S, Herman BA, Wear KA, Harris GR. Development and Characterization of a Tissue-Mimicking Material for High-Intensity Focused Ultrasound. Ieee Transactions on Ultrasonics Ferroelectrics and Frequency Control. Jul.2011 58:1397–1405.
40. Madsen EL, Dong F, Frank GR, Garra BS, Wear KA, Wilson T, et al. Interlaboratory comparison of ultrasonic backscatter, attenuation, and speed measurements. Journal of Ultrasound in Medicine. Sep.1999 18:615–631. [PubMed: 10478971]
41. Pohlhammer, JD., O'Brien, WD, Jr. The Relationship Between Ultrasonic Attenuation and Speed In Tissues and the Constituents: Water, Collagen, Protein, and Fat. New York: Published for the American Association of Physicists in Medicine by the American Institute of Physics; 1980. p. 6
42. Jaejin L, Jeong C, Yang Mo Y, Tai-Kyong S. New clutter rejection method using time-domain averaging for ultrasound color Doppler imaging," in. Ultrasonics Symposium (IUS), 2009 IEEE International. 2009:1371–1374.
43. Reznik N, Williams R, Burns PN. Investigation of vaporized submicron perfluorocarbon droplets as an ultrasound contrast agent. Ultrasound Med Biol. Aug.2011 37:1271–9. [PubMed: 21723449]
44. Kripfgans OD, Fabiilli ML, Carson PL, Fowlkes JB. On the acoustic vaporization of micrometersized droplets. J Acoust Soc Am. Jul.2004 116:272–81. [PubMed: 15295987]
45. Shpak O, Kokhuis TJA, Luan Y, Lohse D, de Jong N, Fowlkes B, et al. Ultrafast dynamics of the acoustic vaporization of phase-change microdroplets. The Journal of the Acoustical Society of America. 2013; 134:1610–1621. [PubMed: 23927201]
46. Doinikov AA, Sheeran PS, Bouakaz A, Dayton PA. Vaporization dynamics of volatile perfluorocarbon droplets: A theoretical model and in vitro validation. Med Phys. Oct.2014 41:102901. [PubMed: 25281982]
47. Wilson K, Homan K, Emelianov S. Biomedical photoacoustics beyond thermal expansion using triggered nanodroplet vaporization for contrast-enhanced imaging. Nature Communications. Jan. 2012 3
48. Viessmann OM, Eckersley RJ, Christensen-Jeffries K, Tang MX, Dunsby C. Acoustic super-resolution with ultrasound and microbubbles. Physics in Medicine and Biology. Sep 21.2013 58:6447–6458. [PubMed: 23999099]
49. O'reilly MA, Hynynen K. A super-resolution ultrasound method for brain vascular mapping. Medical Physics. Nov.2013 40
50. Desailly Y, Couture O, Fink M, Tanter M. Sono-activated ultrasound localization microscopy. Applied Physics Letters. 2013; 103:174107.
51. Huang J, Xu JS, Xu RX. Heat-sensitive microbubbles for intraoperative assessment of cancer ablation margins. Biomaterials. Feb.2010 31:1278–86. [PubMed: 19942283]
52. Asami R, Ikeda T, Azuma T, Umemura S, Kawabata K. Acoustic Signal Characterization of Phase Change Nanodroplets in Tissue-Mimicking Phantom Gels. Japanese Journal of Applied Physics. 2010; 49
53. Vos HJ, Emmer M, de Jong N. Oscillation of single microbubbles at room versus body temperature. 2008 Ieee Ultrasonics Symposium, Vols 1–4 and Appendix. 2008:982–984.

Author Manuscript Author Manuscript Author Manuscript Author Manuscript

54. Forsberg F, Liu JB, Shi WT, Furuse J, Shimizu M, Goldberg BB. In vivo pressure estimation using subharmonic contrast microbubble signals: Proof of concept. Ieee Transactions on Ultrasonics Ferroelectrics and Frequency Control. Apr.2005 52:581–583.

55. Seo M, Matsuura N. Direct Incorporation of Lipophilic Nanoparticles into Monodisperse Perfluorocarbon Nanodroplets via Solvent Dissolution from Microfluidic-Generated Precursor Microdroplets. Langmuir. Oct 2.2014

56. Seo M, Matsuura N. Monodisperse, submicrometer droplets via condensation of microfluidic-generated gas bubbles. Small. Sep 10.2012 8:2704–14. [PubMed: 22700364]

57. Novell A, Arena CB, Kasoji S, Dayton PA. Optimization of multi-pulse sequences for nonlinear contrast agent imaging using a cMUT array. Physics in Medicine and Biology. 2015 vol. In press.

Biographies

Christopher B. Arena was born in Fairport, New York in 1986. He received his B.S. degree in biomedical engineering from the University of Virginia in 2008, and his Ph.D. degree in biomedical engineering from the Virginia Tech – Wake Forest University School of Biomedical Engineering and Sciences. As a graduate student, he worked on developing medical devices for performing therapeutic irreversible electroporation under the direction of Dr. Rafael V. Davalos. With the support of the NIH IRACDA postdoctoral fellowship program, he joined the Dayton lab in the Joint Department of Biomedical Engineering at UNC Chapel Hill and NC State University. His research interests include high-frequency electroporation and nanoparticle-mediated imaging and therapeutic techniques.

Anthony Novell received his M.Sc. degree in medical imaging technologies in 2007 and his Ph.D. in 2011 from the University François Rabelais, Tours, France. He pursued post-doctoral research at the French Institute for Health and Medical Research (Inserm) in Tours, France, under the guidance of Dr. Ayache Bouakaz. He joined Dayton lab at the University of North Carolina, Chapel Hill, NC, in 2014 with the aid of a Post-doctoral Research Fellowship from the ARC Foundation. His research mainly focuses on contrast agent imaging, capacitive micromachined ultrasonic transducers (cMUTs) and therapeutic ultrasound.

Author Manuscript Author Manuscript Author Manuscript Author Manuscript

Paul S. Sheeran was born in Spokane, Washington in 1983. He received dual B.S. degrees in electrical and computer engineering from North Carolina State University in 2007 and received his Ph.D. in 2014 from the joint biomedical engineering department of University of North Carolina and North Carolina State University under the mentorship of Dr. Paul Dayton. Dr. Sheeran is currently a post-doctoral fellow at Sunnybrook Research Institute in Toronto, with research interests including design and characterization of ultrasound-activated contrast agents, development of ultrasound imaging sequences, and therapeutic applications of ultrasound.

Connor Puett received his B.S. in Biomedical Engineering from the University of North Carolina at Chapel Hill in 2013. He is currently a first year medical student in the MSTP-supported M.D.-Ph.D. program at UNC. Prior to graduate school, he worked with Dr. Paul Dayton's group studying the application of phase change contrast agents in diagnostic and therapeutic ultrasound. His research interests lie in the technologies and coding that link diagnostic studies directly with treatment.

Linsey C. Moyer received her B.S. in Bioengineering from Syracuse University in 2005. She was an American Heart Association Pre-Doctoral Fellow during part of her Ph.D. program in Biomedical Engineering at the University of Virginia. After graduating with her PhD in 2011, she went on to accept an NIH IRACDA postdoctoral fellowship at the University of North Carolina at Chapel Hill. After finishing the SPIRE fellowship she moved to Stanford University where she is currently a research associate in the department

Author Manuscript Author Manuscript Author Manuscript Author Manuscript

of Radiological Sciences. Her research interests include MR-guided focused ultrasound and low intensity ultrasound-mediated drug and gene delivery for vascular and oncologic therapeutic applications.

Paul A. Dayton received his B.S. in Physics from Villanova University in 2005, his M.E. in Electrical Engineering from the University of Virginia in 1998, and his Ph.D. in Biomedical Engineering in 2001, also from the University of Virginia. He pursued post-doctoral research and was later research faculty at the University of California at Davis. Much of Dr. Dayton's training was under the mentorship of Dr. Katherine Ferrara, where his initial studies involved high speed optical and acoustical analysis of individual contrast agent microbubbles. In 2007, Dr. Dayton moved to the Joint Department of Biomedical Engineering at UNC Chapel Hill and NC State University, Raleigh, where he is now Professor and Associate Department Chair. Dr. Dayton is currently Associate Director for Education for the Biomedical Imaging Research Center, and his research interests involve ultrasound contrast imaging, ultrasound-mediated therapies, and medical devices. Dr. Dayton is a member of the technical program committee for IEEE UFFC, and a member of the editorial boards for the journals IEEE Ultrasonics, Ferroelectrics, and Frequency Control as well as Molecular Imaging, and Bubble Science, Engineering, and Technology.

Author Manuscript Author Manuscript Author Manuscript Author Manuscript

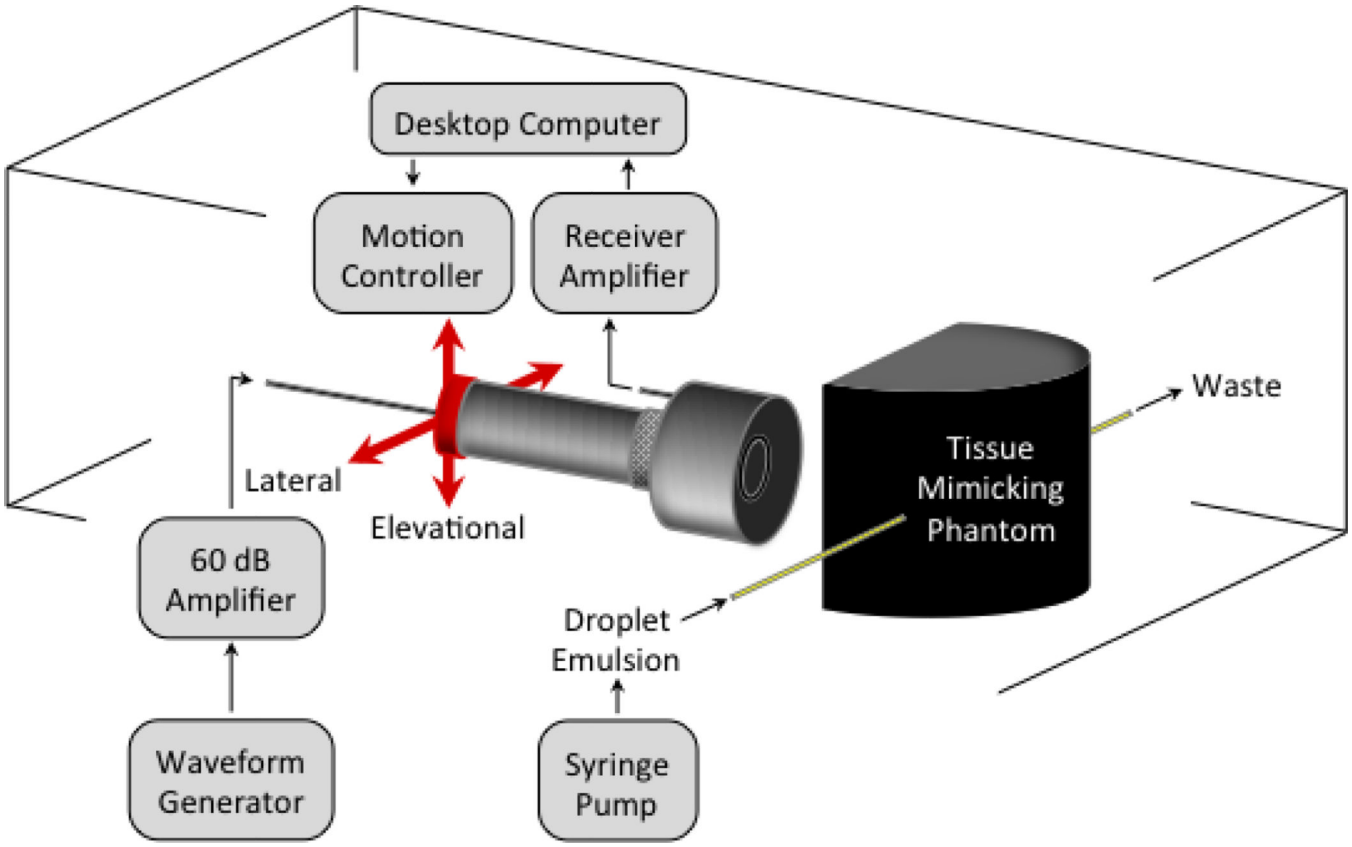

Fig. 1.

Experimental setup. Confocal piston transducers are triggered to transmit (8 MHz, inner element) and receive (1 MHz, outer element) acoustic signals. The location of the transducers is rastered in the lateral-elevational plane to image the tissue-mimicking phantom.

Author Manuscript Author Manuscript Author Manuscript Author Manuscript

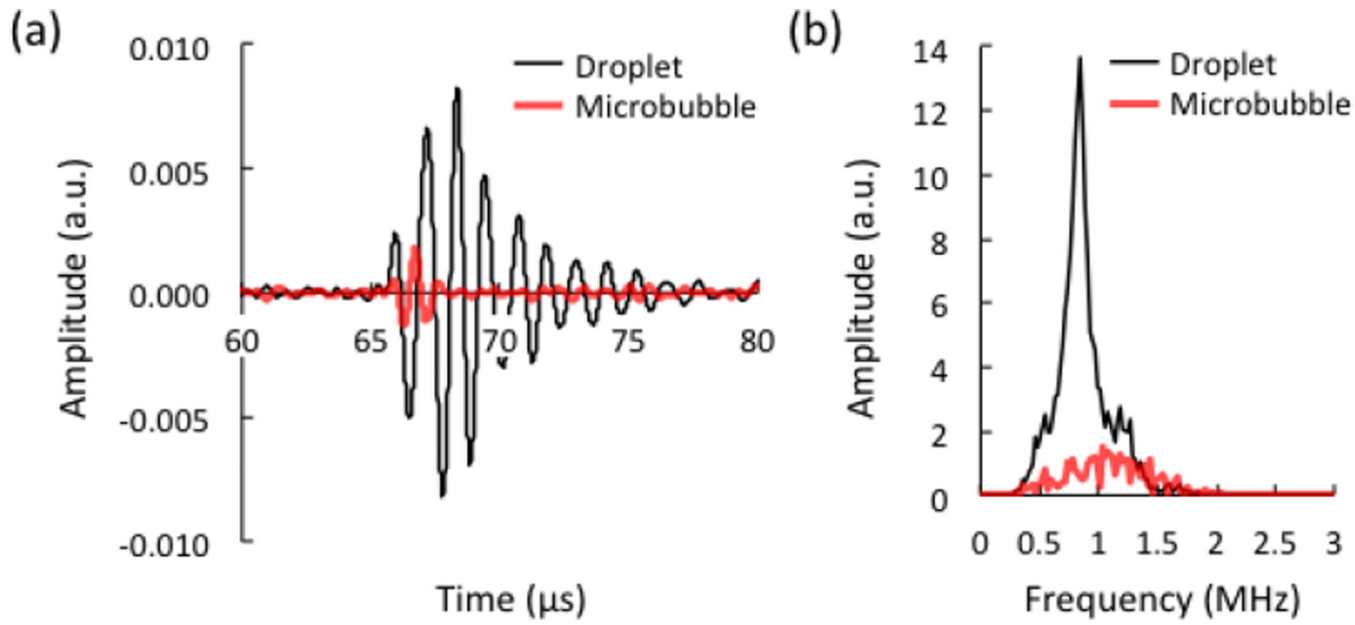

Fig. 2.

(a) Acoustic signals and (b) frequency spectrum from different contrast agents infused through the tissue-mimicking phantom. The concentration of droplets and microbubbles was 0.3%, and the peak negative pressure (PNP) at the focus was 700 kPa. The signals are presented following band-pass filtering (400 kHz to 1.6 MHz), and the magnitude is given in arbitrary units, a.u.

Author Manuscript Author Manuscript Author Manuscript Author Manuscript

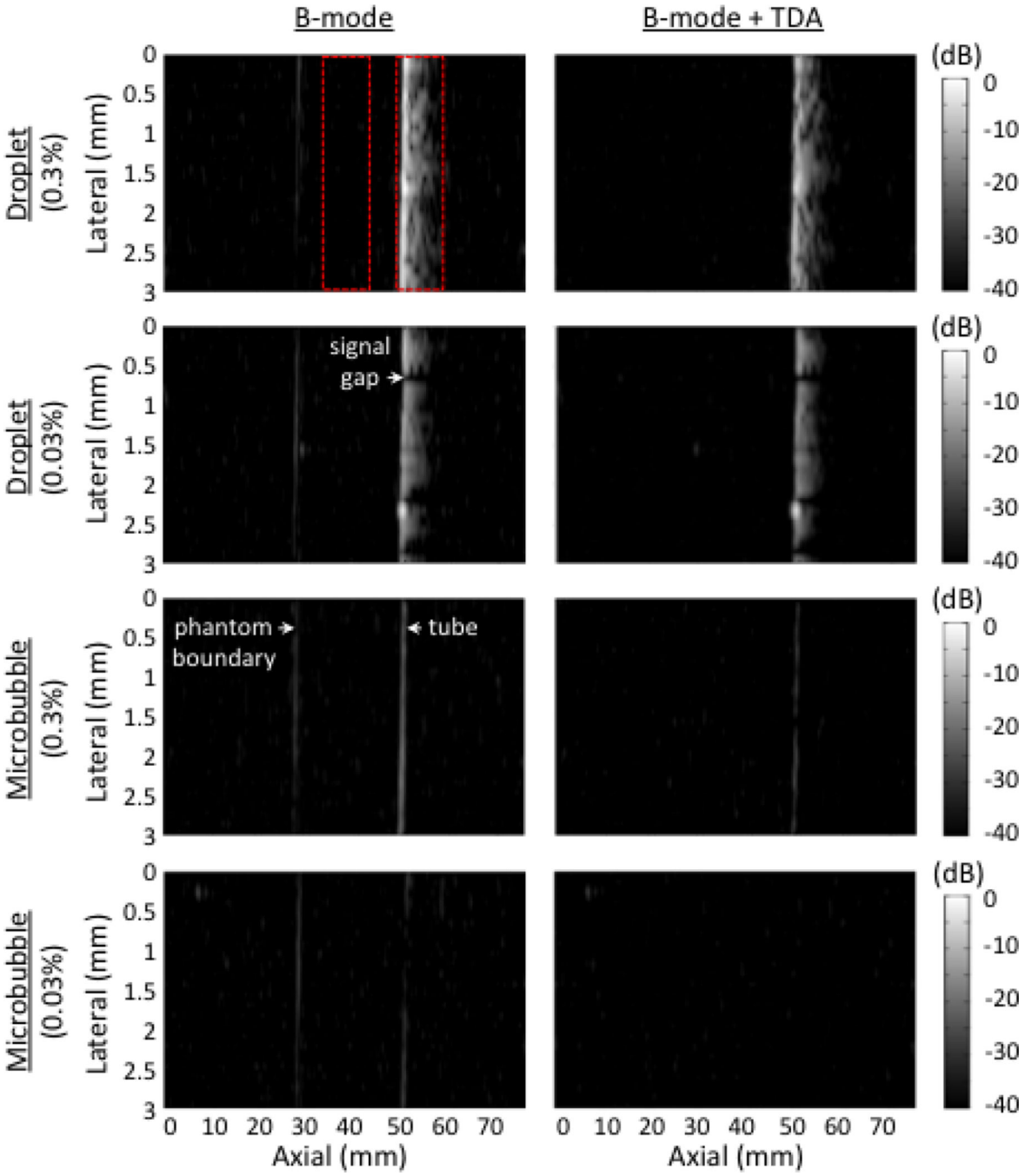

Fig. 3.

B-mode images of various contrast agents infused through the tissue-mimicking phantom. Different concentrations are presented before (left) and after (right) time-domain averaging, TDA. The pressure at the focus was 700 kPa. At that pressure, it was possible to see linear reflections from the water-phantom boundary before TDA. The dynamic range is 40 decibels, dB. Images were normalized to the 0.3% droplet trial pre-TDA. The red dotted areas indicated regions of interest for CTR calculations.

Author Manuscript Author Manuscript Author Manuscript Author Manuscript

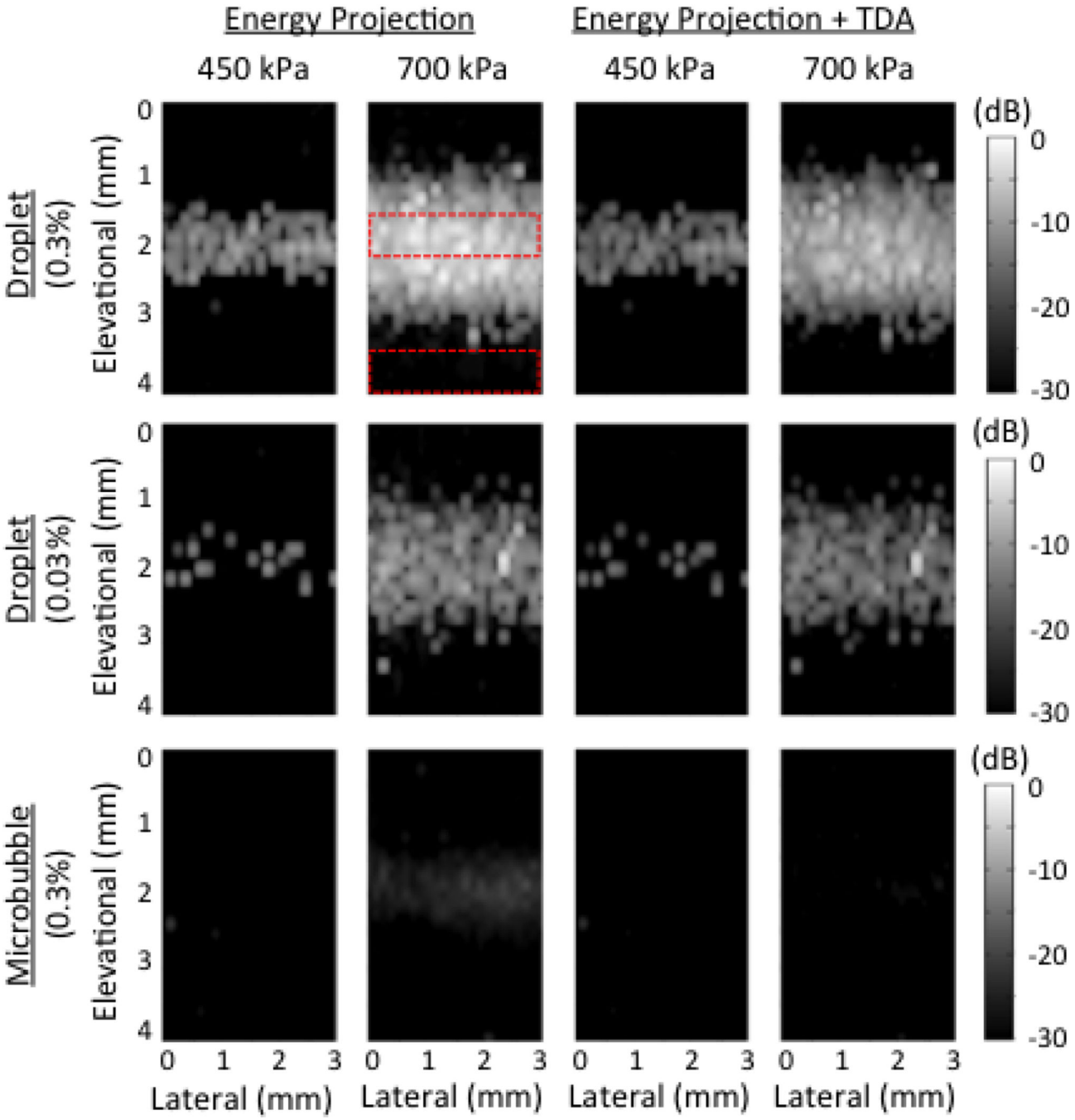

Fig. 4.

Energy projection (EP) images of various contrast agents infused through the tissue-mimicking phantom. Different concentrations and pressures are presented before (left two columns) and after (right two columns) time-domain averaging, TDA. The dynamic range is 30 decibels, dB. Images were normalized to the 0.3%, 700 kPa droplet trial pre-TDA. The red dotted areas indicated regions of interest for CTR calculations.

Author Manuscript Author Manuscript Author Manuscript Author Manuscript

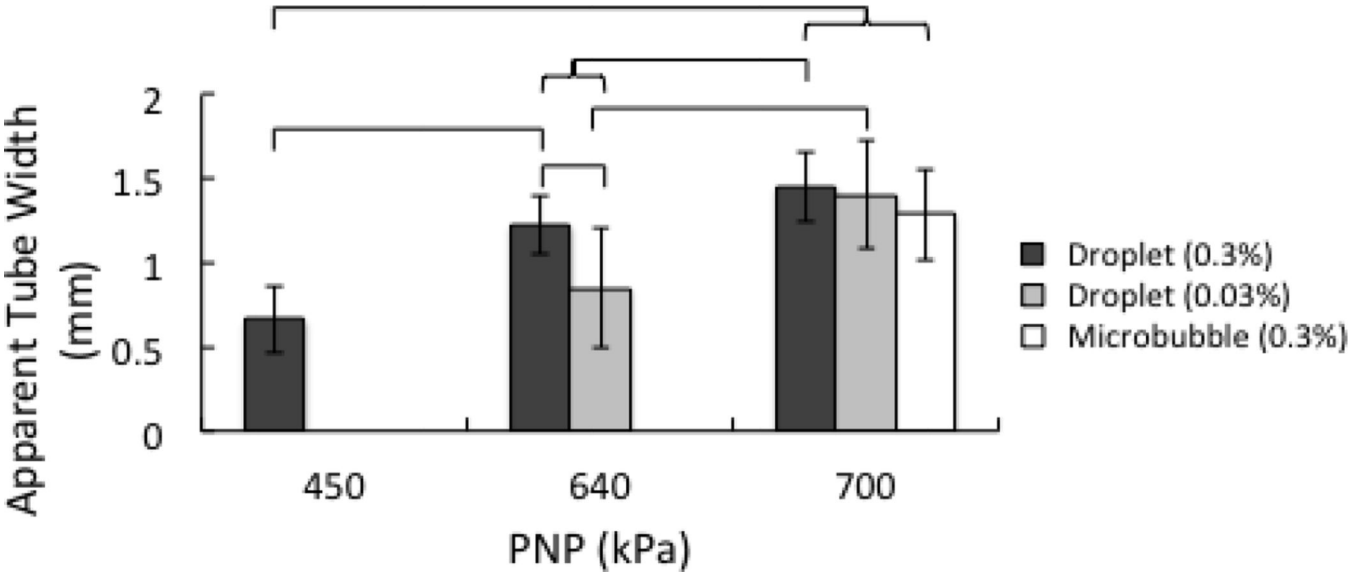

Fig. 5.

Apparent width of the microcellulose tube as a function of contrast agent formulation, concentration, and applied pressure. The error bars indicate one standard deviation. The brackets indicate that a significant difference is present between groups ($p < 0.05$).

Author Manuscript Author Manuscript Author Manuscript Author Manuscript

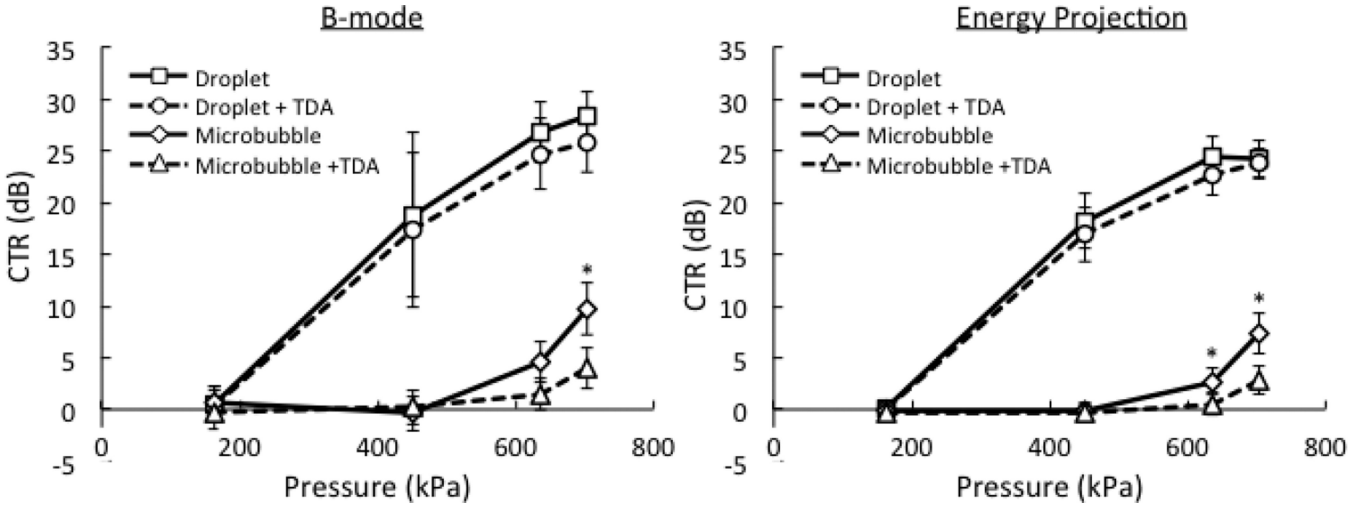

Fig. 6.

Contrast-to-tissue ratio (CTR) for B-mode and energy projection (EP) images as a function of contrast agent formulation and applied pressure. The effects of time-domain averaging (TDA) are shown by the dotted lines. The contrast agent concentration is 0.3%. The error bars indicate one standard deviation. The asterisks denote a significant effect of TDA within droplet or microbubble groups ($p < 0.05$).

Author Manuscript Author Manuscript Author Manuscript Author Manuscript

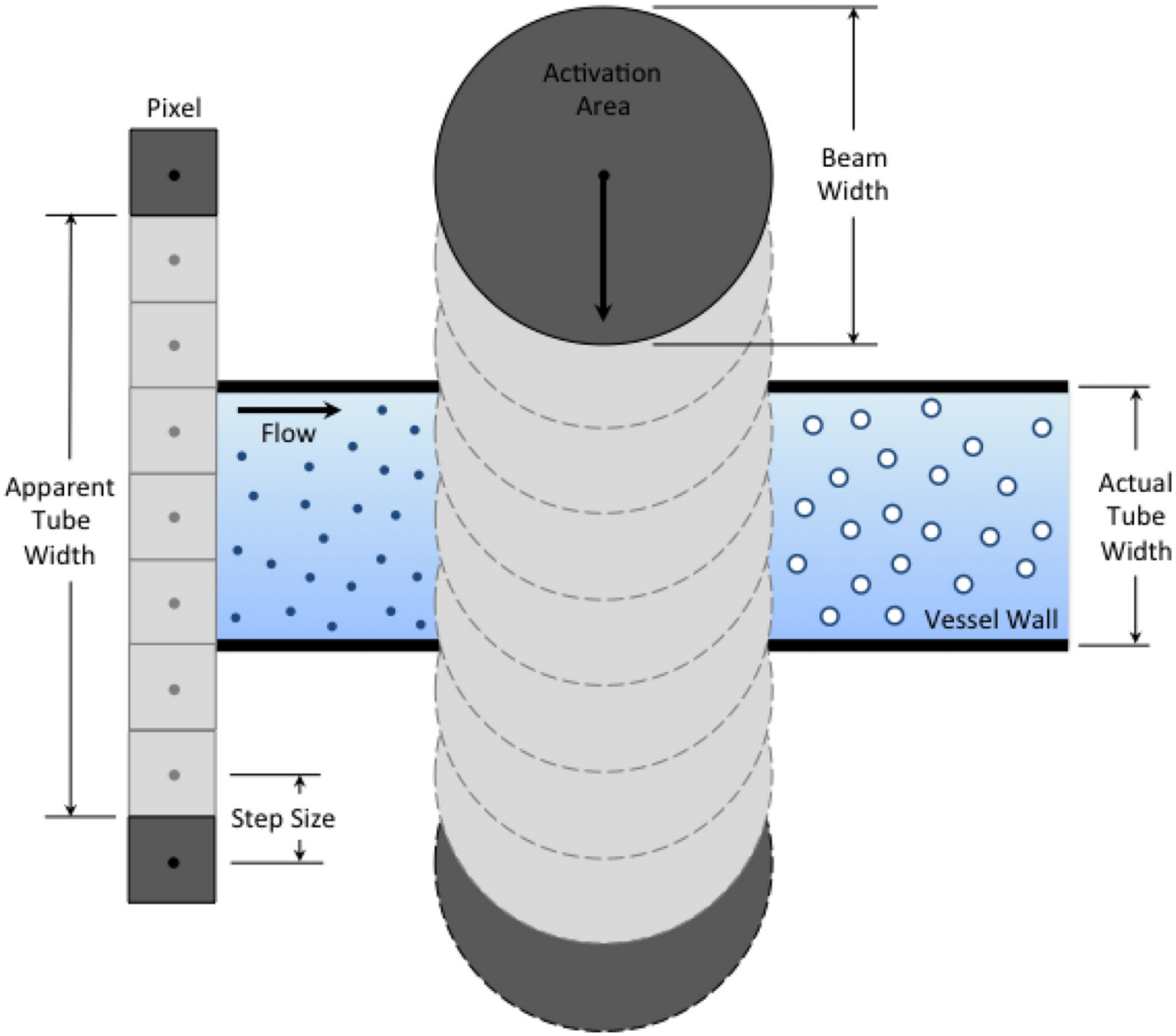

Fig. 7.

Schematic diagram of energy projection (EP) image creation. The apparent tube width is limited by the droplet activation area.

Author Manuscript Author Manuscript Author Manuscript Author Manuscript

TABLE I

Ultrasonic Attenuation of the Phantom

Frequency (MHz)	1	2	3	4	5	6	7	8
Attenuation ($dB.cm^{-1}$)	0.23	0.68	1.26	1.97	2.68	3.35	3.94	4.48

Author Manuscript

Author Manuscript

Author Manuscript

Author Manuscript

TABLE II

Axial Resolution in the Phantom

Contrast Agent	Concentration (%)	PNP (kPa)	Axial Resolution ± Std. Dev. (mm)
Droplets	0.3%	450	3.86 ± 0.73
		640	3.35 ± 1.20[#]
		700	3.28 ± 1.20[#]
Droplets	0.03%	450	3.65 ± 0.82
		640	3.86 ± 0.75[*]
		700	3.56 ± 1.03[*]
Microbubbles	0.3%	640	2.06 ± 0.12[#]
		700	1.91 ± 0.11[#,*]
Microbubbles	0.03%	700	3.18 ± 0.47

[*] indicates a significant difference from 0.3% droplet concentration at equivalent pressures ($p < 0.05$).

[#] indicates a significant difference from 0.03% droplet concentration at equivalent pressures ($p < 0.05$).